Evolutions of Microstructure and Crystallographic Texture in an Fe-1.2 wt.% Si Alloy After (A)Symmetric Warm Rolling and Annealing

Nguyen-Minh, Tuan; Petrov, Roumen H.; Cicalè, Stefano; Kestens, Leo A.I.

Important note
To cite this publication, please use the final published version (if applicable).
Please check the document version above.

Evolutions of Microstructure and Crystallographic Texture in an Fe-1.2 wt.% Si Alloy After (A)Symmetric Warm Rolling and Annealing

TUAN NGUYEN-MINH ●,[1,4] ROUMEN H. PETROV,[1,2] STEFANO CICALÈ,[3] and LEO A.I. KESTENS[1,2]

1.—Department of Electromechanical, Systems and Metal Engineering, Ghent University, Technologiepark 46, 9052 Zwijnaarde, Belgium. 2.—Department of Materials Science and Engineering, Delft University of Technology, Mekelweg 2, 2628CD Delft, The Netherlands. 3.—Rina Consulting, Centro Sviluppo Materiali Spa, Via di Castel Romano 100, 00128 Rome, Italy. 4.—e-mail: Tuan.NguyenMinh@UGent.be

Rolling and annealing is a crucial technology to produce electrical steel sheets. This technology is not just aimed to control the geometry of steel sheets but more importantly to enhance the magnetic properties of the final products via appropriate microstructure and crystallographic texture. In this study, the evolution of microstructures and textures of an Fe-1.2 wt.% Si alloy through the entire processing route (from reheating, warm rolling to annealing) is monitored by electron back-scatter diffraction. Plastic flows of the material during conventional and asymmetric rolling are analyzed in detail based on geometric parameters of the rolling gaps. Deformation textures are accurately predicted by the full-constraint Taylor and advanced Lamel (ALAMEL) crystal plasticity models. The development of recrystallization textures is accounted for by the plastically stored energy in deformed crystals, which in turn is approximated by the plastically dissipated power (i.e., the Taylor factor) as predicted by the full constraint Taylor model. Although asymmetric warm rolling does not produce an improved texture or microstructure for electrical steels, the present study provides useful information on the evolution of the recrystallization microstructure and texture in steels with a complex strain history after asymmetric warm rolling.

INTRODUCTION

Texture and anisotropy are well-known characteristics of polycrystalline metallic materials. Previous studies have demonstrated that the magnetic properties of electrical steels are very sensitive to the crystallographic texture of the finished product.[1,2] As the reference material for soft magnetic cores of electro-magnetic power engines and voltage transformers,[3] electrical steels are essentially pure iron, alloyed with 1.0 wt.% to 6.5 wt.% silicon. Silicon is purposely added to increase the electrical resistance of the materials and thus to reduce the energy loss by eddy currents of magnetic induction cores. For further core loss reduction, electrical steels are commonly produced as electrically insulated thin sheets of about 0.2 mm to 0.5 mm thickness. Therefore, sheet rolling and subsequent annealing are key processes in the production of electrical steels. Controlling the crystallographic texture during material manufacturing has two main objectives. The first objective is to maximize suitable crystallographic orientations, so that the (an)isotropy of properties optimally befits the in-use operational conditions. The second objective of texture control, as a negative imprint of the first, is to reduce and minimize undesired texture components for a given application. In general, texture control of electrical steels by rolling and annealing follows two branches, corresponding to the two main

market grades, namely grain oriented (GO) and non-oriented (NO) grades. Both GO and NO grades are single-phase ferritic steels with a body-centered cubic (BCC) lattice structure, exhibiting the easiest magnetization direction along the $\langle 100 \rangle$ crystallographic axes.[4] According to Beckley,[5] for rotating parts in electro-magnetic devices, since the magnetic field is required to be more homogeneously applied in all directions of the sheet's plane, the most suitable texture in NO electrical steels is the θ-($\langle 001 \rangle$//ND) fiber, which represents the maximum homogeneous density of $\langle 100 \rangle$ orientations in the sheet of the plane. However, obtaining the θ-fiber texture in NO electrical steels by conventional rolling and annealing is far from trivial. Various innovative methods to produce NO electrical steels with the θ-fiber texture have been proposed. Some of them include: manganese removal and decarburization,[6] multi-stage cold rolling with inter-pass annealing,[7] cross rolling[8] and twin roll strip casting.[9] All these advanced methods, although successful in retaining the θ-fiber, are not applicable for large-scale mass production. The manganese removal and decarburization are featured by two subsequent annealing steps. In the first step, the θ-fiber texture is introduced to the sub-surface layers of the material by controlling the chemical composition of annealing atmospheres and the minimization of the surface energy. During the second step, the $\langle 001 \rangle$//ND oriented grains in the sub-surface regions are stimulated to grow inward, thanks to the diffusion of manganese and carbon atoms outward, resulting in a columnar grain structure across the sheet thickness. Because of the requirements on large exposure area and long diffusion annealing periods, surface texture controlling techniques are mostly implemented in batches with a high cost of energy and productivity. The multistage cold rolling with inter-pass annealing, on the other hand, could be applied to massive production with a continuous rolling and annealing line. However, surface quality and particularly homogeneities of microstructure and texture remain problematic issues of the multi-stage cold-rolling and annealing techniques. The cross-rolling technique could result in strongly $\{001\}\langle 110 \rangle$ oriented texture after deformation. The cross rolling, nevertheless, is limited by the width of the rolling mill and thus just applicable as a discontinuous process. Twin roll strip casting, combined with slightly cold rolling and continuous annealing, has shown many benefits for the production of NO-electrical steels, including suitable microstructure and texture. Nevertheless, this technology requires a total re-designing of the processing route, which is uncommonly applicable for existing manufacturing lines. Except for surface texture controlling methods, all above-mentioned techniques require a good understanding of microstructure and texture evolution during rolling and annealing. Additionally, the production of

electrical steels will be more efficient if rolling deformation can be done on a wider range of temperatures.

Therefore, in this paper, the evolutions of texture and microstructure in an iron-1.2 wt.% silicon alloy after warm rolling and annealing are investigated. An elevated rolling temperature has been selected for the beneficial reduction of the deformation stress. On the other hand, it is limited to the critical temperature for the ferrite-austenite phase transformation. Besides conventional rolling, asymmetric rolling has been applied to reduce the thickness of samples and alter the microstructure and texture of the materials. The study includes both experimental measurements and numerical simulations. It is envisioned that the results of the current study will contribute to the understanding of texture evolution during warm rolling and annealing of electrical steels as well as other BCC structured materials.

EXPERIMENTAL AND NUMERICAL METHODS

An Fe-1.2 wt.% Si alloy is the material under investigation in this study. The chemical composition of this material is measured by the inductively coupled plasma (ICP) technique and given in the Table I. The Ae1 and Ae3 temperatures, calculated by the Thermo-Calc^{TM} software with the TCFE5 database, are 961°C and 1028°C. These temperatures are used to select the reheating temperature of warm rolling and the annealing temperature for recrystallization.

The material was first laboratory-casted, reheated at 1200°C and rough rolled at a laboratory mill to obtain the initial thickness of 10 mm. After a second reheating at 900°C for 60 min in pure nitrogen atmosphere, samples were *warm rolled* in three passes to reduce the thickness to 2.0 mm. The reheating temperature of 900°C was selected so that the subsequent rolling deformations were in the single ferritic phase region. The actual rolling temperature, though it could not be measured, is about 200°C lower than the reheating temperature because of the heat loss before the rolling deformation and particularly by the contact of sample and roll surfaces. This rolling temperature is below the ferrite-austenite phase transformation, but it is too high to suppress all single-phase thermal activated processes like dynamic recovery or static recrystallization. The deformation could not be called cold rolling. Therefore, it has been called a warm deformation. Deformation reductions of the three rolling passes were 30%, 43% and 50%, respectively. To maintain the same temperature between different rolling passes, samples were reheated to 900°C for 15 min before each pass. Half of the samples were asymmetrically rolled while the other half was conventionally rolled under the symmetrical condition. During the rolling experiments, the rolling surface and entry directions of the samples were

Evolutions of Microstructure and Crystallographic Texture in an Fe-1.2 wt.% Si Alloy After
(A)Symmetric Warm Rolling and Annealing

Table I. Chemical composition of the studied material

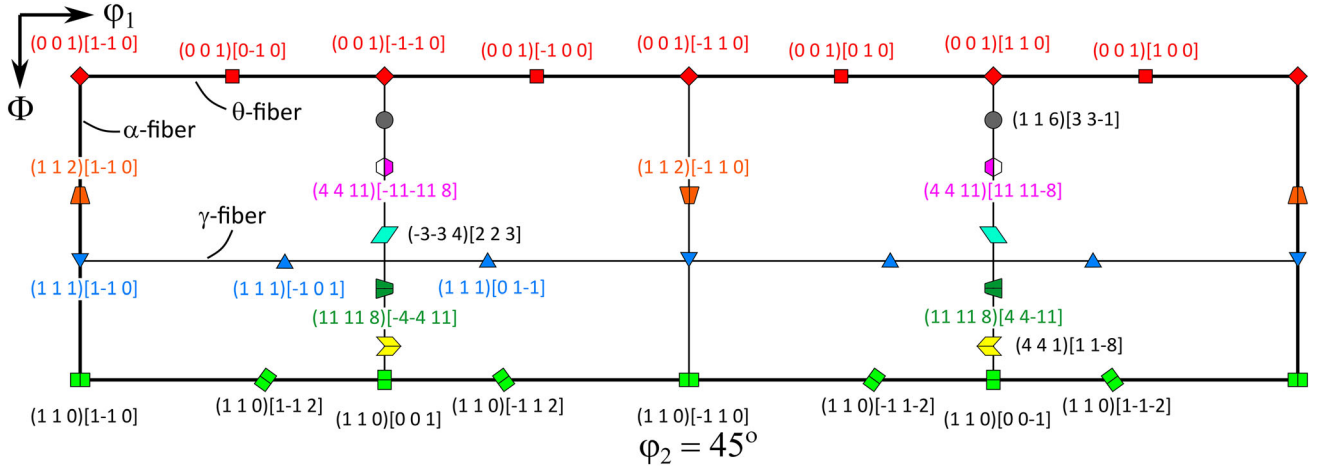| Fe (wt.%)	Si (wt.%)	Mn (wt.%)	Al (wt.%)	Ti (ppm)	C (ppm)	P (ppm)	S (ppm)	N (ppm)
Bal.	1.23	0.31	0.12	20	25	130	80	23

Fig. 1. Locations of important orientations for conventional and asymmetric rolling textures in the $\varphi_2 = 45°$ section of the Euler space.

kept identical. The rolling mill employed in these experiments has the working (top/bottom) roll diameters of 180 mm/180 mm in the symmetric configuration and of 180 mm/125 mm in the asymmetric configuration. Both rolls are driven by separate motors and rotate at the same angular speed. All rolled samples were finally annealed in a furnace with a protective atmosphere at 900°C for 120 min for full recrystallization. Samples for microstructure and texture characterization were collected after each stage of the thermomechanical process, i.e., after reheating, (a)symmetric warm rolling and recrystallization annealing.

To measure the crystallographic texture and microstructure, a field emission gun scanning electron microscope (FEI-Quanta-450^{TM}) equipped with a Hikari EBSD camera (of type EDAX-AMETEK®) has been employed. All samples, after grinding with SiC papers and polishing with diamond suspensions of 3.0 μm and 1.0 μm, were fine polished with a colloidal silica suspension of 0.04 μm for 15 min to remove all artifacts of the sample preparation. Electron backscatter diffraction (EBSD) measurements in the scanning electron microscope have been carried out with an acceleration voltage of 20 kV and a working distance of 16 mm. All EBSD measurements were carried out on a plane perpendicular to the sheet transverse direction (TD-plane) with the sheet rolling direction (RD) being horizontal. The stage moving strategy combined with a fine EBSD scanning step size, down to 0.5 μm, allows combining wide field observations with high spatial resolution. For each sample, crystallographic orientations and grain areas of at least 5000 grains were measured. A grain in an EBSD microstructure is defined as an enclosed crystal domain by boundaries of 15° misorientation. After the measurements, EBSD microstructures and textures have been analyzed by the OIM Analysis^{TM} v7.3 software (EDAX-AMETEK®).

To calculate crystallographic textures from orientation data collected by EBSD measurements, Gaussian functions with a half-width of 7.0° were superimposed for each data point, and the ODF was expressed as a series expansion of spherical harmonics with the highest expansion coefficient of order 22.[10] Crystallographic orientation distribution functions (ODFs) are calculated without imposing any sample symmetry, implying that the range of the three Euler angles extends over $0° \leq \varphi_1 \leq 360°$ and $0° \leq \Phi, \varphi_2 \leq 90°$. By applying this rule to all ODF calculations, differences between textures of conventional and asymmetric rolling are easy to visualize. Because of the difference in rolling configurations, textures of asymmetrically rolled samples only have the TD axis as two-fold axis, which results in a pole figure exhibiting a mirror plane perpendicular to TD. Contrarily, since the RD, TD and ND of conventionally rolled samples are two-fold axes, the pole figure exhibits three mirror planes normal to all three sample reference axes (i.e., RD, TD and ND). For convenience of texture analysis, ODFs of both conventionally and asymmetrically rolled samples are presented in the conventional $\varphi_2 = 45°$ section. Locations of important components of (a)symmetric rolling textures in the $\varphi_2 = 45°$ ODF section are shown in Fig. 1.
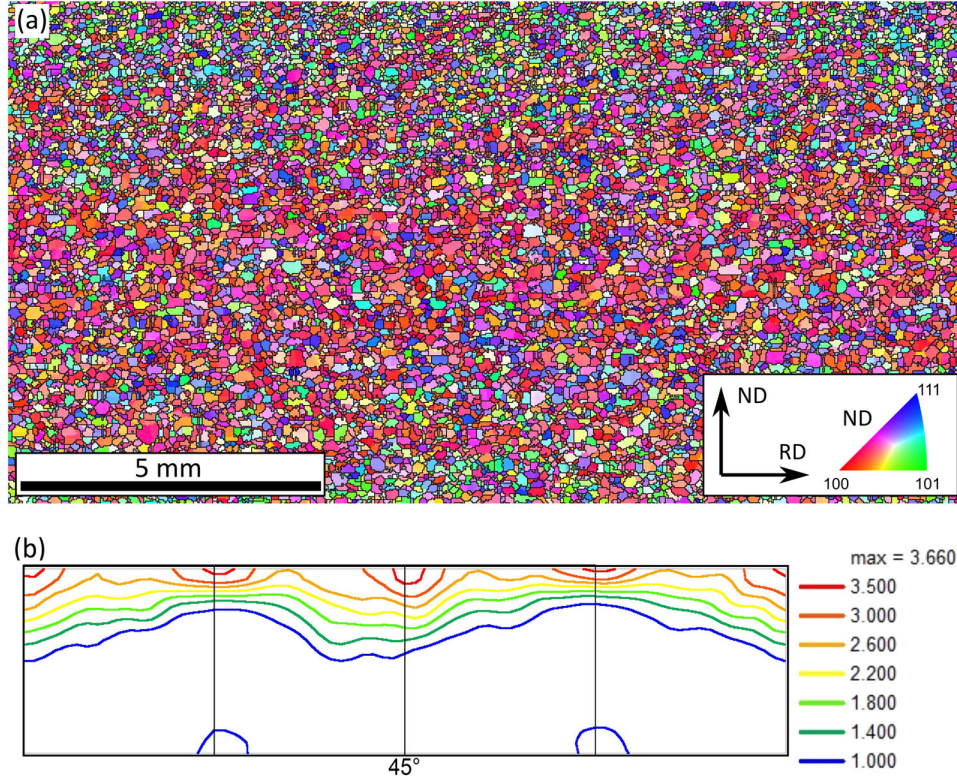
Fig. 2. (a) ND-IPF map and (b) φ_2 = 45° ODF section of the initial sample after rough rolling from 1200°C and annealing at 900°C for 60 min in a pure nitrogen protective atmosphere.

To account for texture formation in warm-rolled samples, crystal plasticity simulations with the full constraints Taylor (FCT)[11] and the advanced Lamel (ALAMEL)[12] models are carried out. The initial ODF is discretized to 2000 individual orientations by a statistically cumulative method, proposed by Toth and Van Houtte.[13] Crystal plasticity during warm rolling is resolved by optimizing multi-slip activity of three different types of slip systems (i.e., {110}, {112} and {123}⟨111⟩). The critical resolved shear stresses of all slip families are initially equal and follow a linear hardening law corresponding to the total amount of accumulated slip. Both differential hardening between slip systems and latent hardening are ignored; hence, the hardening does not interfere with the selection of optimum slip systems. Large strain deformation is simulated in a stepwise mode with small strain increments of 0.5% accumulating to the macroscopically imposed deformation. Results of crystal plasticity simulations including Taylor factor and lattice rotation rates are employed to analyze texture evolutions after plastic deformation and recrystallization annealing. The MTM-FHM software suit[14] is employed for ODF calculation and simulation of deformation textures.

RESULTS

Microstructure and Texture of the Initial Sample

Figure 2 shows the ND inverse pole figure (ND-IPF) map and the φ_2 = 45° ODF section measured on a sample after rough rolling and annealing for 60 min at 900°C, i.e., the stage just before warm rolling. Because of the thickness of 10 mm and the weak texture intensities on an annealed sample, a total area of 32,000 × 10,000 μm^2 on the RD-ND plane was measured by EBSD with a scanning step size of 10 μm on a square grid. The initial microstructure (see Fig. 2a) consists of equiaxed grains with average grain size diameter of 133 μm (SD = 43 μm). The absence of in-grain orientation gradients in this microstructure indicates that lattice defects responsible for such gradients such as geometrically necessary dislocations are strongly reduced after annealing at 900°C for 60 min. The spatial distribution of crystals across the sheet thickness is not homogeneous. Grains in the mid-thickness region (the center horizontal region of Fig. 2a) are larger than the ones near the sample surfaces (the regions closed to the top and bottom
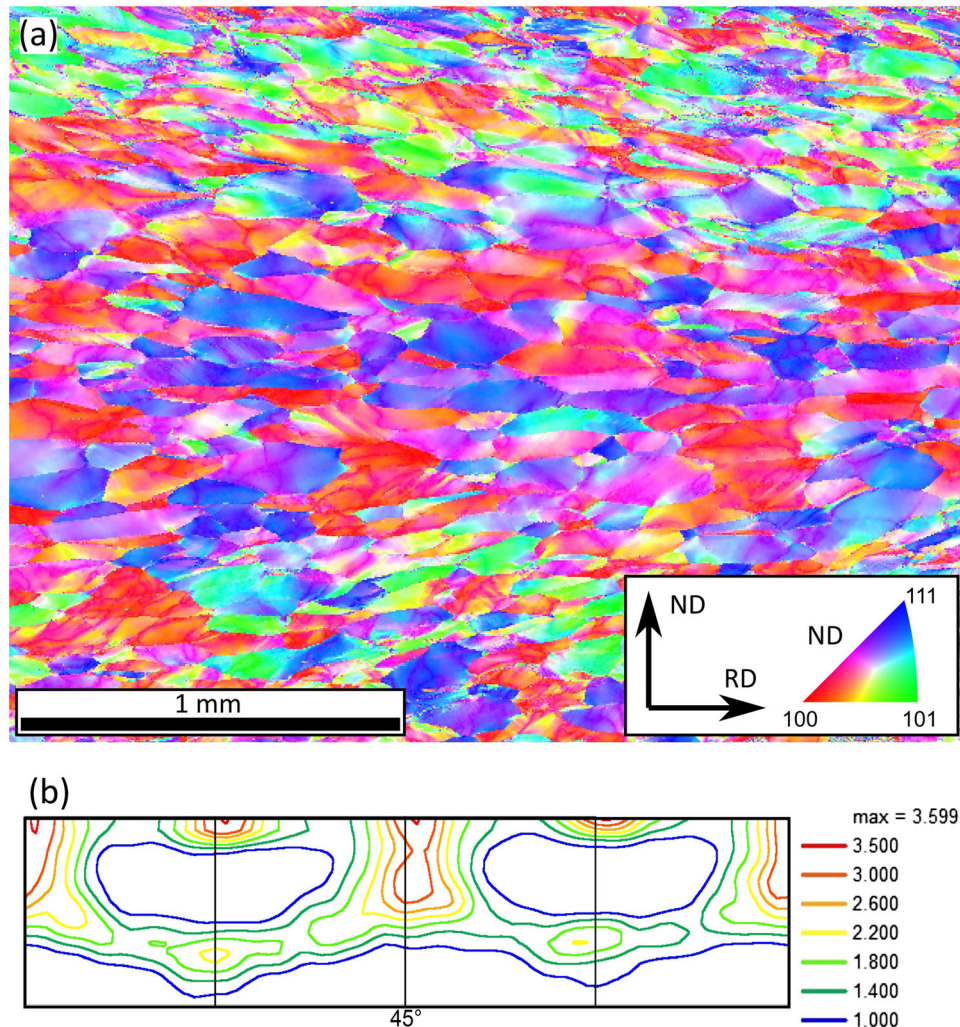
Fig. 3. (a) ND-IPF map and (b) $\varphi_2 = 45°$ ODF section measured across the 2.0 mm thickness of a conventionally warm-rolled sample.

edges of Fig. 2a). Crystallographic orientations of the grains in the mid-thickness region are mostly of the ⟨001⟩//ND orientations, although a few grains with the ⟨111⟩//ND orientations are also visible in the same region. The ⟨011⟩//ND-oriented grains, on the contrary, are frequently present near the sample surfaces.

The macroscopic texture of the rough rolled sample (see Fig. 2b) is rather weak. The maximum intensity in this texture is about 3.5 multiples of random density (mrd). This highest texture intensity peak is measured at the rotated Cube ({001}⟨110⟩) orientation. From this highest intensity peak, the ODF spreads toward the Cube ({001}⟨100⟩) orientation, and not to the E-({111}⟨110⟩) orientation as usually observed in ODFs of conventionally rolled samples. The intensity of the Cube texture component is 2.7 mrd while texture intensity near the E-component is below the random level. The Goss ({110}⟨001⟩) orientation is also observed in the same ODF with an intensity of 1.2 mrd. This texture component corresponds to the ⟨011⟩//ND fiber observed near the sample surfaces

as indicated previously (see Fig. 2a). In general, the spread of the ODF from the {001}⟨110⟩ to the {001}⟨100⟩ components, although it is not as homogeneous as for an ideal θ-fiber, looks very promising for texture control in NO electrical steels. It suggests the possibility to produce NO electrical steels with Cube fiber texture just by conventional rolling and annealing. For the current sample, the high thickness of 10 mm makes it unsuitable to be employed as iron core lamellar sheet because the energy core loss due to eddy currents will be far too high as it is proportional to the square of the thickness (d^2). Therefore, to reduce the gauge further processing is required.

Microstructure and Texture in Conventionally Warm-Rolled Samples

The microstructure and crystallographic texture in a sample after conventional warm rolling are shown in Fig. 3. The ND-IPF map (c.f. Fig. 3a) shows a microstructure of flat elongated grains which exhibit smooth variations of crystallographic

orientation. The grain morphology and crystallographic orientations of $\langle 011 \rangle$//RD and $\langle 111 \rangle$//ND in the mid-thickness region are consistent with deformation microstructures and textures of conventionally warm-rolled samples. The occurrence in the sub-surface layers of $\langle 011 \rangle$//ND-oriented grains with a long axis inclined with respect to the rolling direction suggests a different deformation condition for grains in these layers. Because of the high friction between working rolls and sample surface during warm rolling, the strain mode of the crystal orientations near the sample surface is affected by the presence of simple RD-ND shear strain (SS) as opposed to plane strain compression (PSC) in the mid-thickness region. SS results in the orientation preference of the Goss ($\{110\}\langle 001 \rangle$) and Copper ($\{112\}\langle 111 \rangle$) orientations. It depends on the magnitude of the shear compared to the compressive strain, whether shear texture components (i.e., the Goss and Copper orientations) appear as the dominant components of the macroscopic texture of conventionally warm-rolled sheet. Specifically, in the ODF of Fig. 3b, the texture intensity of the Goss orientation is below the random level and the Copper orientation is completely absent from the ODF. Contrarily, high texture intensity peaks of this ODF are located along the α- ($\langle 110 \rangle$//RD) fiber, with the two highest peaks of 3.6 and 3.0 mrd near the rotated Cube ($\{001\}\langle 110 \rangle$) and the I-($\{112\}\langle 110 \rangle$) orientations.

The ODF, in general, exhibits orthorhombic sample symmetry, although this symmetry was not imposed during the texture calculation. The presence of the orthorhombic sample symmetry in the ODF reveals a deformation configuration of PSC for conventional rolling. Compared to those of the α-fiber texture components, intensities of the γ-($\langle 111 \rangle$//ND) fiber texture components are relatively weak. All components of the latter fiber have intensities < 2.0 mrd. The spread of the ODF along the γ-fiber toward the Goss orientation results in a local high intensity peak of 2.0 mrd near the D^*-($\{11\ 11\ 8\}\langle 4\ 4\ 11 \rangle$) orientation.

Microstructure and Texture in Asymmetrically Warm-Rolled Samples

To change the microstructure and texture of the rolled samples, warm asymmetric rolling was carried out. Figure 4a shows the through-thickness microstructure of such an asymmetrically warm-rolled sample with the top surface contacting to the larger diameter roll. Compared to the conventionally warm-rolled sample, (c.f. Fig. 3a), the microstructure of the asymmetrically rolled one is more homogeneous. Grains with elongated and inclined shapes are observed in all regions across the sample thickness. Grain orientations are

homogeneously scattered across the sample thickness, and there is no sharp distinction between the mid-thickness and sub-surface regions as in the case of conventional rolling. All these microstructural features suggest the presence of a homogeneous strain across the sample thickness during asymmetric rolling. Moreover, this through-thickness microstructure is like the one near the surfaces of conventionally rolled samples. Therefore, an extension of shear strain across the sample thickness could explain the microstructure evolution in the asymmetrically rolled samples.

The macroscopic texture of the asymmetrically rolled sheet, as can be seen on the $\varphi_2 = 45°$ ODF section (c.f. Fig. 4b), is remarkably different from that of the conventionally rolled sheet. Generally, the ODF of conventionally rolled sheet exhibits three two-fold sample symmetry axes corresponding to the RD, TD and ND. In the $\varphi_2 = 45°$ ODF section (e.g., Fig. 3b), this two-fold symmetry of the RD is revealed by a mirror line along the $\varphi_1 = 180°$ axis, while the two-fold character of the TD is manifested by two symmetry lines along $\varphi_1 = 90°$ and $\varphi_1 = 270°$. For asymmetric rolling, only the TD retains a two-fold axis; thus, in the $\varphi_2 = 45°$ section of the ODF, only the mirror lines at $\varphi_1 = 90°$ and $\varphi_1 = 270°$ remain, cf. Fig. 4b). Therefore, the ODF of asymmetrically rolled samples should be analyzed in the regions between the TD mirror symmetry axes at $\varphi_1 = 90°$ and $\varphi_1 = 270°$.

Along the TD mirror symmetry axes, the ODF of asymmetric rolling has three high-intensity peaks near the $(\overline{3}\overline{3}4)[223]$, $(116)[33\overline{1}]$ and $(441)[11\overline{8}]$ texture components. Among these peaks, the one near the $(441)[11\overline{8}]$ orientation has the highest texture intensity of 3.6 mrd. The texture intensities near the $(116)[33\overline{1}]$ and $(\overline{3}\overline{3}4)[223]$ orientations are 3.4 and 2.6 mrd, respectively. The texture components of the α- and γ-fiber are not observed in this ODF. Instead, the intensity spread from the $(441)[11\overline{8}]$ component towards the RD//$\langle 110 \rangle$ at $\varphi_1 = 180°$ and $\varphi_1 = 360°$ forms a fiber texture, which can be interpreted as a shift towards higher Φ-angles of the well-known γ-fiber texture of conventional rolling. A shift of other high intensity peaks in the asymmetric rolling texture from the corresponding positions in the conventional rolling texture is also observed. The $(116)[33\overline{1}]$ component in the asymmetric rolling texture is rotated $13.3°$ away from the rotated Cube orientation, while the $(441)[11\overline{8}]$ component is $19.5°$ away from the $(11118)[44\overline{11}]$ orientation of the conventional rolling texture. Both shifts are along the $\varphi_1 = 270°$ axis toward higher Φ-angles. Alternatively, the rotation of the $(\overline{3}\overline{3}4)[223]$ orientation from the $(\overline{11118})[4411]$ orientation of the conventional rolling texture is $17.2°$ along the $\varphi_1 = 90°$ axis toward lower Φ-angles.
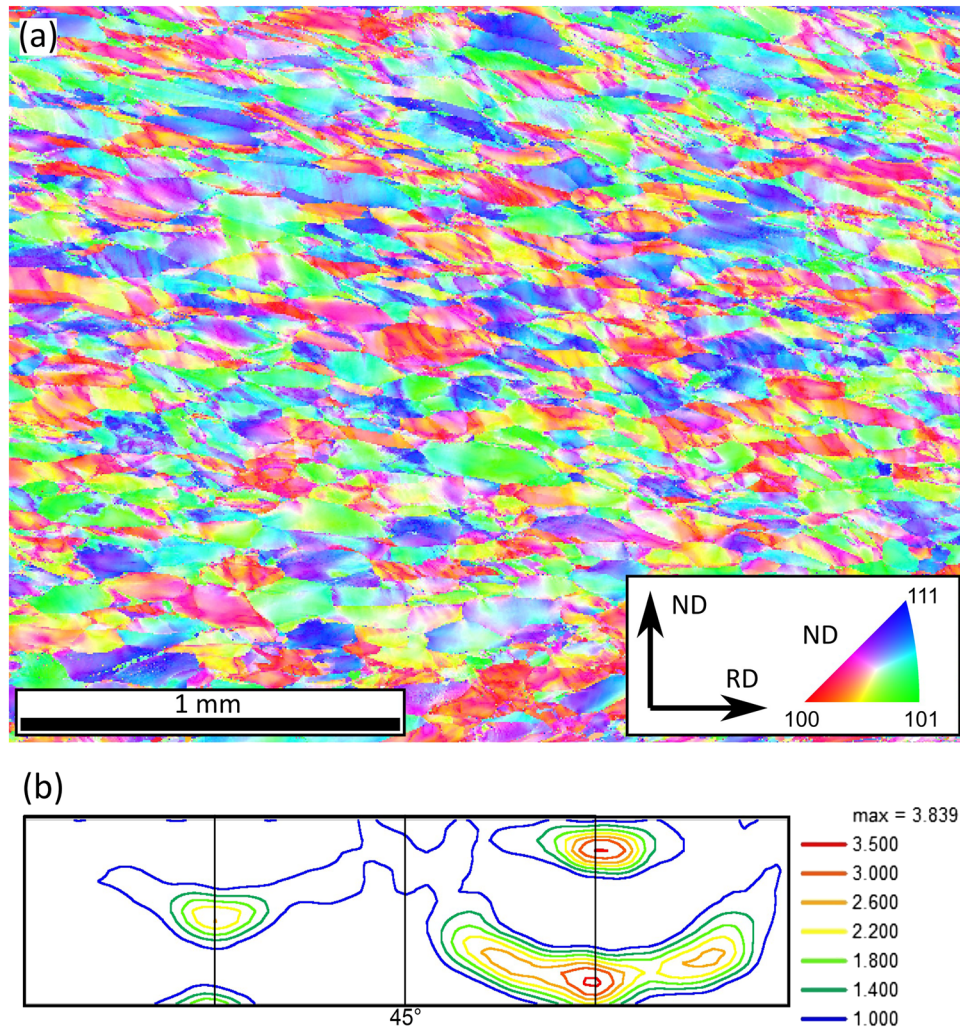
Fig. 4. (a) ND-IPF map and (b) $\varphi_2 = 45°$ ODF section measured across the 2.0 mm thickness of an asymmetrically warm-rolled sample.

Microstructure and Texture in Conventionally Rolled and Annealed Samples

To investigate the effect of different deformation conditions on the formation of the recrystallization microstructure and texture, samples after warm rolling were annealed at 900°C for 120 min in a protective atmosphere for full recrystallization. The microstructure of a sample after conventional warm rolling and annealing (see Fig. 5a) exhibits grains of polygonal shape. Most of the grains have an equiaxed morphology, although some grains in the mid-thickness region are slightly elongated along the RD. The average grain size diameter (c.f. Fig. 5b) measured across the sample thickness is 130 μm (SD = 53 μm). Grains in the mid-thickness region are larger than those near the sample surfaces. All grains in this microstructure have sharply defined orientations with internal orientation gradients < 5°. Also, the variation of grain orientations across the sample thickness is rather limited. Orientations of the $\langle 110 \rangle$//ND fiber are more frequently observed in the sub-surfaces than in the mid-thickness region.

The macroscopic texture of conventionally rolled and annealed samples is given in Fig. 5c. Compared to the deformation texture after warm rolling, this annealing texture has significantly weakened. The highest texture intensity peak in this ODF is located near the rotated Cube component with an intensity of 2.8 mrd. This cross-thickness texture (c.f. Fig. 5c) is dominated by the α-fiber and the D^*-({11 11 8}$\langle 4\ 4\ 11 \rangle$) texture components. Wide spreads of the ODF from this highest intensity peak along the α-fiber and toward the Cube ({001}$\langle 100 \rangle$) texture components are also visible. Intensities of all texture components in the ODF region from the Cube toward the rotated Cube and the I-({112}$\langle 110 \rangle$) orientations are > 1.5 mrd. In this recrystallization texture, the D^*-({11 11 8}$\langle 4\ 4\ 11 \rangle$) component appears as a local intensity maximum of 1.7 mrd.
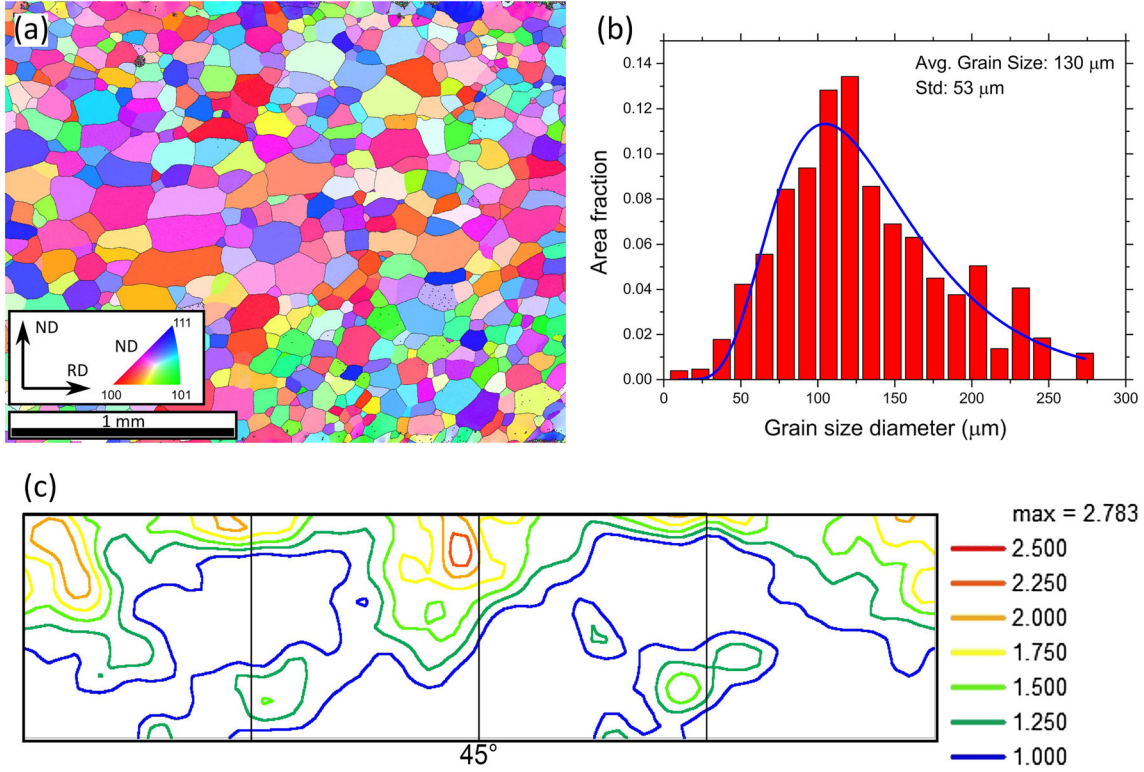
Fig. 5. (a) ND-IPF map, (b) grain size histogram and (c) $\varphi_2 = 45°$ ODF section measured across the thickness of a conventionally warm-rolled samples after annealing at 900°C for 120 min in a protective atmosphere.

Microstructure and Texture in Asymmetrically Rolled and Annealed Samples

Figure 6 shows microstructure and crystallographic texture of a sample after asymmetric warm rolling and annealing. The microstructure (c.f. Fig. 6a) is similar to the one after conventional rolling and annealing (c.f. Fig. 5a). Polygonal and equiaxed grains dominate the microstructure and are homogeneously distributed across the sample thickness. The average grain size diameter (c.f. Fig. 6b) is 110 μm (SD = 41 μm), which is slightly smaller than the one observed after conventional rolling and annealing. All grains in the microstructure exhibit a unique crystallographic orientation without internal orientation spread, and there are no visible orientation gradients across the sample thickness.

The macroscopic cross-thickness averaged texture of an asymmetrically warm-rolled sample after the recrystallization annealing is shown in Fig. 6c. Because of the peculiar nature of this texture, its quantitative analysis is not convenient since none of the high-intensity peaks correspond to familiar rolling texture components. Miller indices of these orientations are mostly shown by multi-digit numbers and do not reflect the real crystallographic plane and direction of the material. Therefore, this recrystallization texture will be analyzed with orientation coordinates represented by Euler angle triplets (φ_1, Φ, φ_2) instead of the Miller indices.

The first remarkable feature of the $\varphi_2 = 45°$ section of Fig. 6c is the statistical sample symmetry of this recrystallization texture. The mirror symmetry lines along the $\varphi_1 = 90°$ and $\varphi_1 = 270°$ axes are visible in the ODF section, which indicates that the monoclinic sample symmetry with TD as two-fold axis, induced by asymmetrical rolling, is preserved. The second feature which can be observed in this recrystallization texture is the presence of sparse and weak local maxima. The highest intensity peak in this ODF is 2.9 mrd, which is observed near the orientation with Euler triplet (270°, 18°, 45°). The location of this maximum is very near to one of the strongest texture components in the deformation texture of the asymmetrically warm-rolled sample, namely the $(116)[33\bar{1}]$ orientation, cf. Fig. 4b. The angular deviation between the deformation and recrystallization components is about 5° around the TD axis. Another component of the recrystallization texture, which is in the vicinity of a local maximum of the deformation texture, is the orientation with Euler angles (90°, 49°, 45°). This orientation is about 2° away from the $(\bar{3}\bar{3}4)[223]$ orientation of the deformation texture. Conversely, the $(441)[11\bar{8}]$ orientation, which has the highest
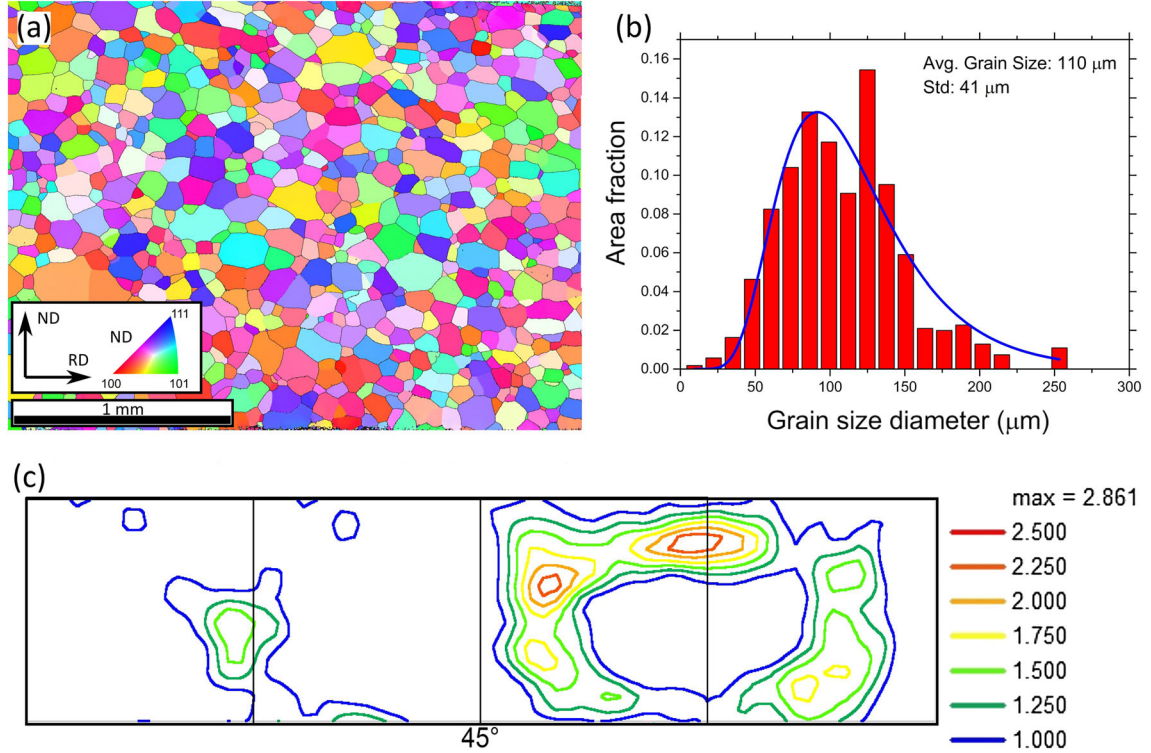
Evolutions of Microstructure and Crystallographic Texture in an Fe-1.2 wt.% Si Alloy After (A)Symmetric Warm Rolling and Annealing

Fig. 6. (a) ND-IPF map, (b) grain size histogram and (c) $\varphi_2 = 45°$ ODF section measured across the thickness of an asymmetrically warm-rolled sample after annealing at 900°C for 120 min in a protective atmosphere.

intensity in the asymmetric rolling texture, does not appear in the recrystallization texture. The second highest intensity peak in the recrystallization texture is located on the position with Euler triplet (213°, 35°, 45°) with an intensity of 2.4 mrd, which does not bear any relation with a maximum of the deformation texture. The most remarkable feature in the texture of asymmetrically rolled and annealed sample is the fiber-type spread of intensity. The continuous scatter of the ODF intensity from the (270°, 18°, 45°) orientation toward the two symmetric variants of the (213°, 35°, 45°) components and gradually decreasing toward the Goss (270°, 90°, 45°) orientation forms an O-ring type fiber, which is rather atypical for rolling and recrystallization textures.

DISCUSSION

Deformation Mode of the Material During Warm Rolling

To understand the evolution of the crystallographic texture after plastic deformation, it is necessary to know the displacement field applied to the material during the deformation. For conventional rolling, it is well known that plane strain compression is an appropriate approximation of the macroscopic deformation condition. According to Dieter and Bacon,[15] reduction of the thickness when a sample runs through the rolling gap results in a

compressive strain along the ND and a corresponding extension in the RD. Widening along the TD during conventional rolling is commonly neglected, when the width of samples is significantly larger than the thickness. The compressive strain (ε_{33}) along the ND and tensile strain (ε_{11}) along the RD during conventional rolling are determined by the ratio of the initial (h_i) and the final (h_f) thickness of the sample:

$$\varepsilon_{11} = -\varepsilon_{33} = \ln\left(\frac{h_i}{h_f}\right) \qquad (1)$$

In this first approximation, the strain tensor calculation for conventional rolling is rather simple because it is nothing more than a purely geometric model of the rolling gap. Neither real time nor the complex deformation path of the material between entering and exiting of the rolling gap is consider. Also the appearance of a texture gradient across the thickness could not be accounted for by the homogeneous PSC approach. The effect of friction between working rolls and sample surface and the impact of rolling velocity are equally ignored by the simplified approach of Eq. 1.

In fact, the presence of Goss-oriented grains near the top and bottom surfaces of conventionally rolled samples indicates the existence of RD-ND shear strains (ε_{13}) in the sub-surface regions. It can be asserted, though, that the magnitude of these shear

strains should be rather small since the Goss component is observed in the microstructure but the intensity of this component in the thickness averaged ODF is below the random level.

Alternatively, the homogeneous distribution of differently oriented grains across the thickness and particularly the absence of the RD as a two-fold axis in the texture of the asymmetrically rolled sample suggest the major role of RD-ND shears during asymmetric rolling. To purposely introduce RD-ND shear strains, Lee[16] has proposed various configurations of asymmetric rolling. All implementations of asymmetric rolling, despite their configurational differences, are intended to produce samples deformed by a high amount of shear strain distributed homogeneously across the sample thickness. The two factors that have the most impact on RD-ND shear strains are friction on the sample surfaces and the rolling speeds of working rolls regarding the forward speed of the sheet. Apart from these two factors, the penetration depth of the shear strain and thus the homogeneity of crystallographic texture across the sample thickness are also dependent on the hardening evolution in the material. In the current study, since the rolling experiments have been carried out at elevated temperature (900°C), it is believed that the strain hardening is sufficiently low and thus a through-thickness penetration of the RD-ND shear strain will not be suppressed.

The friction between rolls and material during warm or hot rolling, in general, is much higher than during cold rolling, which conventionally occurs under well-lubricated conditions. The friction and hardening evolution of the material in the present experiment are similar for both conventional and asymmetric rolling. The last and therefore the most crucial factor resulting in microstructure and texture differences between conventional and asymmetric rolling is the rolling speed. In the case of conventional rolling, the rotational velocity of working rolls is identical. Therefore, the occurrence of the RD-ND shear in conventionally rolled samples is merely due to small differences of rolling velocity between material layers parallel to the rolling plane. Additionally, when the flatness of conventional rolling is maintained, the RD-ND shear will be balanced in the mid-thickness region of the samples.

In the case of asymmetric rolling, although the rotational velocity of working rolls is identical, the difference in roll diameters leads to a higher rolling velocity for the larger roll and vice versa. By assuming the sliding between rolls and sample is negligible, Kang et al.[17] have estimated the RD-ND shear strain (ε_{13}) of asymmetric rolling from roll diameters (R_1 and R_2), the initial (h_i) and final (h_f) thickness of the sample as follows:

$$\varepsilon_{13} = \frac{1}{h_i + h_f}\left[R_1\mathrm{acos}\left(\frac{2R_1 - h_i + h_f}{2R_1}\right) - R_2\mathrm{acos}\left(\frac{2R_2 - h_i + h_f}{2R_2}\right)\right] \quad (2)$$

Therefore, a sample, when proceeding through the rolling gap of the asymmetric rolling mill, will be subjected to both compressive strain because of the imposed thickness reduction and shear strain because of the difference of rolling velocities between the top and bottom rolls. By applying Eqs. 1 and 2, the nominal strain tensor components of asymmetric rolling can be estimated. In the present work, the texture evolution during asymmetric as well as conventional rolling will be calculated by the FCT and the ALAMEL models using the strain tensor values given by Eqs. 1 and 2.

Deformation Textures Predicted by Crystal Plasticity Models

According to Eq. 1, the compressive strains that were imposed in the current experiment during the three consecutive rolling passes of both conventional and asymmetric rolling are 0.36, 0.56 and 0.69, respectively. In addition to these compressive strains, the amounts of RD-ND shear strains imposed during the three asymmetric rolling passes are 0.16, 0.25 and 0.37, respectively. These values of the strain tensor components and particularly the ratio between shear and compressive strain components ($\varepsilon_{13}/\varepsilon_{33}$) for asymmetric rolling increase monotonically with the number of rolling passes. Previous study by Sidor et al.[18] suggests that the deformation condition during the last rolling pass is more important to the formation of crystallographic texture than during the previous passes. Therefore, in this study, it is assumed that after the first and second passes the material may have (partially) recrystallized and result in a very weak recrystallization texture. This near random texture is considered the starting texture prior to the third pass.

Deformation textures predicted by the FCT and the ALAMEL models, as can be observed in Fig. 7, exhibit different features between conventional and asymmetric rolling. Specifically, for the simulated textures of conventional rolling (c.f. Fig. 7a and b), orientation preferences to the α- and the γ-fiber texture components are predicted by both the FCT and the ALAMEL models. Unsurprisingly, the $I(\{112\}\langle110\rangle)$ and D^*-($\{11\ 11\ 8\}\langle4\ 4\ 11\rangle$) orientations are present in these simulated ODFs with the highest intensity peaks. The rotated Cube texture component, although visible in the experimental ODFs, only appears as a local maximum in the FCT modelled texture. Simulated textures of asymmetric rolling as predicted by the two models (c.f. Fig. 7c and d) exhibit one of the highest intensity peaks near the $(\overline{3}\overline{3}4)[223]$ texture component. Components of the α- and the γ-fiber textures are not present in these simulated ODFs. However, the spreads of the ODF from the $(441)[11\overline{8}]$ orientation toward the RD at $\varphi_1 = 180°$ and $\varphi_1 = 360°$ axes, as observed in the measured texture of Fig. 4b, also appear in the simulated ones. Therefore, differences between textures of conventional and asymmetric
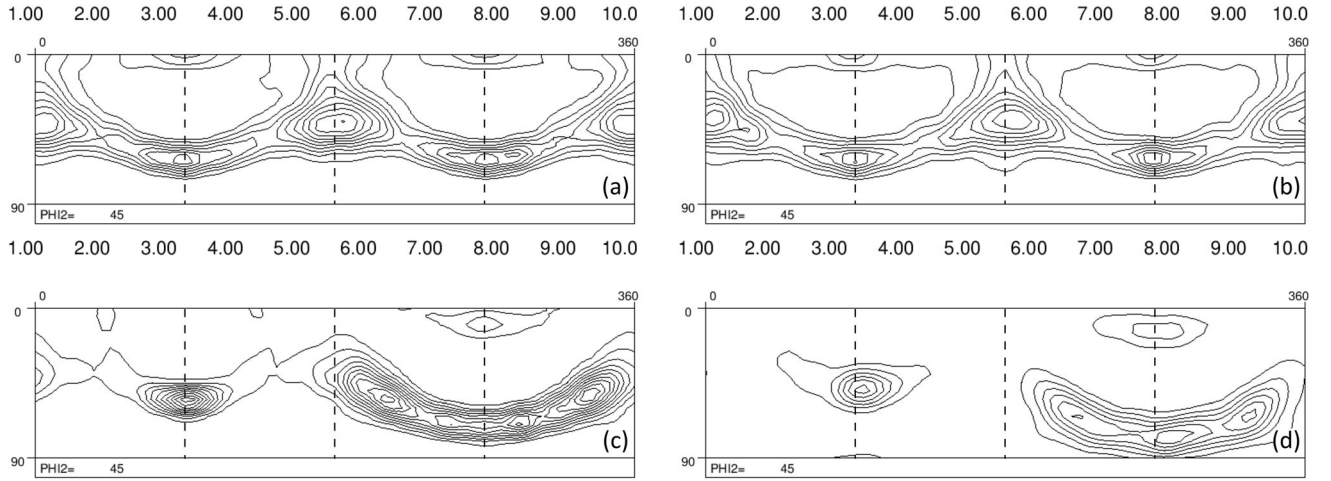
Fig. 7. $\varphi_2 = 45°$ ODF sections of deformation textures after (a, b) conventional rolling and (c, d) asymmetric rolling; predicted by (a, c) the FCT model and (b, d) the ALAMEL model.

rolling could be accounted for by the presence or absence of RD-ND shear in the strain tensor applied to the material during rolling.

Simulated textures by the FCT and ALAMEL model for conventional and asymmetric rolling, in general, resemble the measured ones (c.f. Figs. 3b and 4b). To measure the fit between simulated and measured textures and to evaluate the predictive quality of crystal plasticity models, the texture indices of the difference ODF (TI_{dODF}) for each pair of one simulated ($f_{sim}(g)$) and the corresponding measured texture ($f_{mea}(g)$) could be calculated. Mathematically, the normalized texture index of the difference ODF is defined by Van Houtte et al.[12] as follows:

$$TI_{dODF} = \frac{\oint (f_{mea}(g) - f_{sim}(g))^2 dg}{\oint (f_{mea}(g))^2 dg} \qquad (3)$$

Generally, values of the TI_{dODF} are in the range of 0 to $+\infty$, and the smaller value of the TI_{dODF}, the better the similarity between the two compared ODFs is. According to Eq. 3, the differences between the measured texture of conventional rolling and corresponding simulated textures by the FCT and the ALAMEL models are 1.12 and 0.81, respectively. In the case of asymmetric rolling, the differences between measured and simulated textures by the two models are 1.52 and 0.74, respectively. Hence, the texture prediction quality of the ALAMEL model is suggested to be better than that of the FCT model for both conventional and asymmetric rolling. Because the initial simulation condition for both models is identical, differences between simulated textures can be exclusively assigned to the differences between the crystal plasticity models.

In the FCT model, it is well known that the crystals of the polycrystalline aggregate are individually and uniformly subjected to the straining condition as experienced by the macroscopic sample.[19] This full constraint condition is appropriate for single-crystal plasticity and in cases whereby interactions between neighboring grains during plasticity could be negligible, e.g., because of geometrical identical shapes of the grains. Under such deformation conditions, the crystal orientations are not restricted by geometric grain boundaries. However, in most of the polycrystalline materials, grains are limited in their displacement by the boundaries with their neighbors, and neighboring grain interactions across the grain boundaries are important microstructural features. Therefore, the ALAMEL model considers the plastic accommodation of pairs of grains and allows stress relaxation by equal but opposite shears at either side of the common boundary segment. By considering grain boundaries during crystal plasticity, the ALAMEL model, proposed by Van Houtte et al.,[12] maintains the stress equilibrium on the shear relaxation plane and the strain compatibility between crystals at the boundary plane. Plastic energy in this model is distributed proportionally between the two grains, and a part of this energy is absorbed by grain boundaries via stress relaxation on the grain boundary plane. All these considerations produce slower and more realistic crystal rotations during deformation than the ones predicted by the FCT model. The effect, indeed, can be observed from the simulated textures in Fig. 7. Not only the shapes of the ODFs but also the texture intensities predicted by the ALAMEL model are nearer to the measured ones, whereby it can be observed that the maxima of the ALAMEL modeled texture are of lower intensity than the maxima of the FCT modeled counterpart. The ALAMEL model provides the better prediction of deformation textures for both conventional and asymmetric rolling compared to the FCT model.

Formation of Recrystallization Textures

To account for the evolution of crystallographic textures in warm-rolled and annealed samples, it is necessary to understand the recrystallization mechanisms and to differentiate them from other thermally activated processes.[20] Primary recrystallization involves the formation of a new grain structure in a deformed material by the formation and migration of high-angle grain boundaries driven by the stored energy of deformation.[21] Migration of low-angle grain boundaries, though contributing to nucleation of primary recrystallization, rarely produces detectable changes of crystallographic texture and therefore will not be further discussed. The recrystallization texture, accordingly, is a function of high-angle grain boundary migration and distribution of deformation stored energy in crystals. The evolution of the recrystallization texture, consequently, will be discussed in terms of these two aspects especially in terms of their orientation dependence.

Recrystallization textures of both conventional and asymmetric rolling in this study are analyzed in terms of the corresponding deformation textures because recrystallization and corresponding deformation textures are closely related.[22] During rolling, crystal grains are rotated toward preferred orientations under the prescribed straining condition. Plasticity of crystal orientations during rolling is accommodated by dislocation glide. Interaction and accumulation of dislocations result in lattice defect structures. The presence of dislocation structures produces elastic distortions of crystal lattices and thus leaves a small fraction of strain energy in the crystal grains after deformation. According to Rollett et al.,[20] this stored energy, though less than 10% of the total energy spent to plastically deform the material, is the main driving energy for recrystallization. Dislocation slip and thus the density of dislocations after plastic strain are orientation dependent.[23] The storage of energy in deformed crystals, therefore, is affected by straining directions of the crystals. Accurate quantitative measurement of dislocation densities of individual deformed crystals, however, remains a challenging task. Various efforts have been spent on measuring the dependence of plastic stored energy on crystallographic orientation of deform crystals.[22] Results of these studies, nevertheless, are merely available for specific materials under well-known deformation modes, for instance, of the IF steel after conventional cold rolling.[24] Moreover, simulations on dislocation structures of deformed crystals are limited to some specific cases because of the highly computational cost of the current dislocation dynamic models. Effects of the stored energy in deformed crystals on the formation of recrystallization texture, therefore, have not yet been fully evaluated.

Crystal plasticity models, for instance the FCT model, do not calculate the plastically stored energy but evaluate the instantaneous plastic energy dissipation in a crystal by dislocation slip. The dissipated plastic energy to activate slip could be represented by the Taylor factor (M). Mathematically, this factor is measured by the ratio of the rate of plastic power dissipated by the activity of all slip systems to the plastic work rate in a unit volume of crystal.[25] Assuming a unit strain rate is applied to the polycrystalline aggregate, the Taylor factor map, for a prescribed deformation condition, could be obtained by the FCT model results.

Figure 8 shows the Taylor factor maps in the $\varphi_2 = 45°$ Euler section of Euler space for conventional and asymmetric rolling under consideration in this study. These Taylor factor maps exhibit surprisingly matching features with the corresponding ODF sections of the recrystallization texture. Both for conventional and asymmetric rolling, high texture intensity peaks of the recrystallization ODFs coincide with the locations of low Taylor factor regions. For conventional rolling, the correspondence of the Taylor factor map (see Fig. 8a) to the initial texture rough rolled texture (c.f. Fig. 2b) is even better than to the annealing texture after warm conventional rolling (c.f. Fig. 5c). It must be noticed, though, that the initial texture before conventional rolling is also a recrystallization texture issued after the preceding rough rolling process. The differences between the recrystallization textures after rough rolling and finish rolling (c.f. Figs. 2b and 5c) may be due to a variety of reasons, for example, a drastically different initial texture prior to the rolling operation or a difference in rolling reduction of the last pass. Nevertheless, this is clear evidence of the fact that the formation of recrystallization textures in both conventional and asymmetric warm rolling is to enhance the recrystallization of low Taylor factor orientation.

The recrystallization textures in this study (c.f. Figs. 2b, 5c and 6c) are mostly composed of dispersed and weak intensity peaks. The dominant texture components of recrystallization textures are just revealed in measured ODFs of large area samples. All recrystallization textures are measured on areas of square centimeter scale, but the maximum texture intensities in these ODFs are not higher than 3.6 mrd (with a Gaussian spread of 7° on each individual orientation). The average grain size diameters in the annealed microstructures are of the order of 100–130 μm. The formation of large-sized grains requires long distance migrations of grain boundaries whereby small and fragmented grains of the deformed matrix are consumed by large and defect-free crystals in the recrystallization microstructure.[20] Because grain boundary migration is a thermally activated process, as indicated by

Evolutions of Microstructure and Crystallographic Texture in an Fe-1.2 wt.% Si Alloy After (A)Symmetric Warm Rolling and Annealing
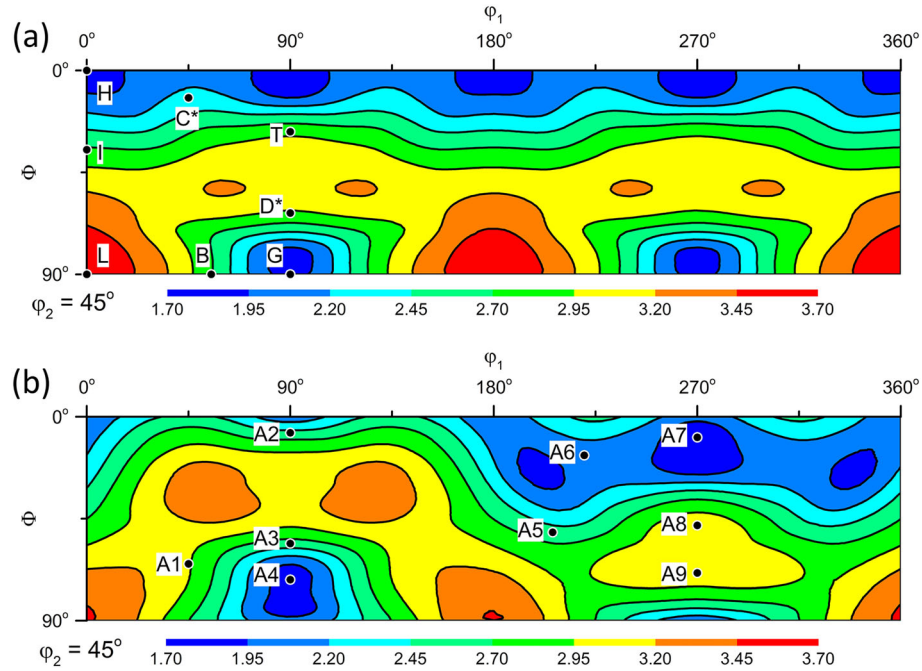

Fig. 8. The Taylor factor maps on $\varphi_2 = 45°$ Euler sections calculated by the FCT model for a BCC structured material under (a) PSC of conventional rolling and (b) PSC + SS of asymmetric rolling.

Gottstein and Shvindlerman,[26] there are higher annealing temperature and the larger grain boundary mobility and thus larger grain size after annealing. Moreover, grain boundaries inherit structural characteristics from their composing crystals and exhibit anisotropy on their migration rates. Therefore, the crystallographic orientations of growing grains will appear as main components of the recrystallization texture. However, for the formation of primary recrystallization texture, the anisotropy of grain boundary mobility is usually a minor factor compared to differences in plastically stored energy among deformed crystals. Hence, the evolution of the primary recrystallization texture is crucially influenced by the stored energy distribution rather than by the mobility anisotropy of grain boundaries.

To illustrate the relationship between the plastically stored energy and the formation of recrystallization texture components, texture calculations based on orientation selection by Taylor factor value can be done, as reported by Kestens and Jonas[27] and Sidor et al.[28] Recrystallization texture prediction by these models, however, requires detailed parameter selection as well as necessary calibration steps. For illustration purposes in this work, a simple calculation procedure is introduced. Rolling textures, as shown in Figs. 3b and 4b, are discretized in 10,000 individual orientations, distributed homogeneously in Euler space. The discrete orientations have been used as input data for recrystallization texture

calculations. The rough rolling texture before recrystallization, as it was not measured, was assumed to be the same as the conventional warm rolling texture (Fig. 3b) but with just half the intensity as the rough rolling reduction was only 20% compared to the 80% of conventional warm rolling reduction. Crystallographic orientations of the three rolling conditions are selected or rejected for recrystallization depending on the Taylor factor values under the corresponding deformation conditions. All crystal orientations in the rough rolling and asymmetric rolling samples with a Taylor factor among the 20% lowest values are selected and considered recrystallized grains. To account for the recrystallization texture in conventionally warm-rolled samples, it is necessary to include orientations of the 50% lowest Taylor factor as components of the recrystallization texture. These different critical Taylor factors to select/reject oriented crystals are accounted for by various initial textures and non-uniform recrystallization rates among samples. The selection of low Taylor factor orientations for the recrystallization texture, indeed, implies the preference of low stored energy nucleation.

Although it is beyond the scope of this study to discuss the low and the high stored energy nucleation, it is necessary to emphasize the dependence of the two opposed nucleation mechanisms on the deformation temperature. After plastic deformation at elevated temperatures, the low stored energy recrystallization nucleation frequently occurs and
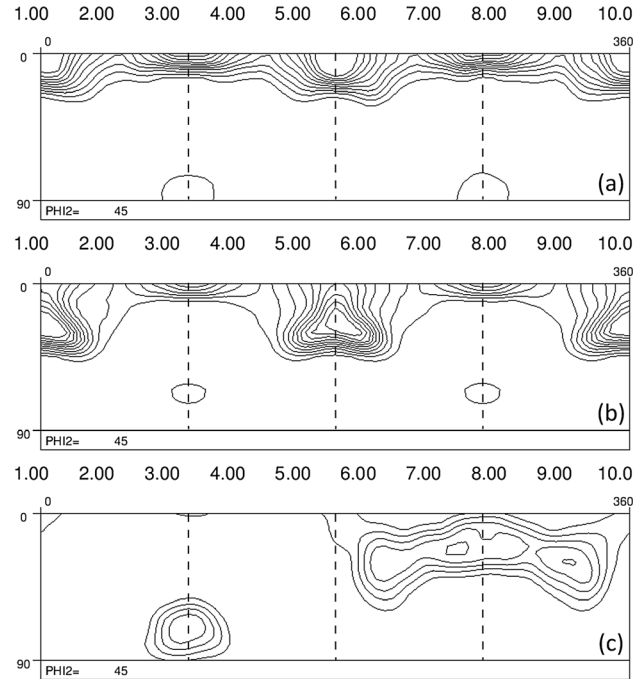
Fig. 9. The $\varphi_2 = 45°$ ODF sections to account for the formation of recrystallization textures in (a) a rough-rolled sample, (b) a conventionally rolled sample and (c) an asymmetrically rolled sample. Crystallographic orientation components in the deformation textures are selected based on their Taylor factor values.

vis-versa.[29] Because of the high mobility of dislocations during plastic deformation at elevated temperatures, plastic work and presumably stored energy within oriented grains are homogeneously distributed. In-grain heterogeneities in warm-deformed samples occur less frequently than in cold-deformed samples. Abnormal growth of sub-grains within high stored energy crystals, for instance, of the $\langle 111 \rangle$//ND oriented grains, has less chance to develop in warm-rolled and annealed samples. Alternatively, strain-induced boundary migration of sub-grains at boundary regions of the low stored energy crystals (e.g., the $\langle 001 \rangle$//RD grains) becomes energetically advantageous.[30] As a result, the recrystallization textures of warm-deformed sample are composed of low Taylor factor orientations.

Figure 9 shows the three $\varphi_2 = 45°$ ODF sections as predicted recrystallization textures for rough rolling, warm conventional and asymmetric rolling, based on a simple Taylor factor criterion. For all warm-rolling experiments, only orientations from the discretized deformation texture were selected that do not exceed a critical threshold of $P_{0.2}$ for the rough-rolled and asymmetrically rolled material and $P_{0.50}$ for the conventionally warm-rolled material. The main features of the recrystallization textures are indeed reproduced in the calculated ODFs. The Taylor factor of crystal plasticity theory, although simple and dimensionless, is an appropriate parameter to estimate orientation dependence of stored energy in deformed crystals and therefore can be employed to quantitatively estimate the evolution of recrystallization textures.

Although it was attempted by asymmetric warm rolling to obtain an improved magnetic quality of the recrystallization texture, i.e., a texture with a higher intensity of the $\langle 100 \rangle$//ND fiber (the θ-fiber), this goal was not achieved. Because of the detrimental combination of PSC and SS strain modes, the distribution of stored energy in Euler space turns out to be off the $\langle 100 \rangle$ fiber (cf. Fig. 8b). The textures observed after conventional symmetrical rolling, either after rough rolling (cf. Fig. 2b) or after finish rolling warm rolling (cf. Fig. 5b), are more suitable for magnetic purposes than the textures obtained by asymmetrical finish rolling. The fact that the rough-rolled texture is even of somewhat better quality than the conventionally warm-rolled texture has to do with the fact that the presumed deformation texture of the rough-rolled slab, before final recrystallization, is far weaker than the rolling texture after conventional warm rolling (Fig. 3b). In this case the nucleation mechanism in the rough rolled material nearly sampled from a quasi-random texture, which explains why the annealing texture of Fig. 2b very much resembles the lower domains of the Taylor factor map of Fig. 8a.

CONCLUSION

In this study, the evolutions of microstructure and crystallographic texture in an Fe-1.2 wt.% Si alloy after warm rolling and annealing are investigated. By applying asymmetric rolling, as opposed to conventional symmetric rolling, an atypical texture evolution has been observed.

Evolutions of deformation and recrystallization textures, in general, are dependent on straining condition of the material. For conventional rolling, a small variation in rolling speeds results in the presence of RD-ND shear strain just near the sample surfaces. Goss oriented grains, therefore, are observed in sub-surface layers of the conventionally rolled sample, but texture intensity of this component is still below the random level. In the case of asymmetric rolling, due to the difference in working roll diameters, the RD-ND shear strain is present across the sample thickness resulting in a non-conventional deformation texture, significantly different from the α- and γ-fiber texture of the conventional rolling. The deformation textures in conventional and asymmetric rolling can be reliably predicted by crystal plasticity simulations with the FCT and the ALAMEL models. The ALAMEL model, thanks to the consideration of grain interaction in crystal plasticity, produces better texture predictions than the FCT model.

Recrystallization microstructures, when considered as emerging from the plastically deformed state, are conditioned by the substructure and crystallographic features ensuing after warm rolling. Because of the difference in strain modes between conventional and asymmetric rolling, deformation textures and thus recrystallization textures are significantly different. The recrystallization texture is mainly controlled by the orientation dependence of the plastically stored energy of the deformed crystals. For the warm-rolled samples in this study, the development of the recrystallization texture is characterized by the nucleation of low stored energy orientations. The orientation dependence of the plastically stored energy in deformed crystals was estimated by the Taylor factor as predicted by the full constraint Taylor model It could clearly be observed that the dominant components and even the fine structure features of the recrystallization textures were determined by the characteristics of the Taylor factor distribution in Euler space, i.e., the low Taylor factor domains coincide with the preferred orientation domains of the recrystallization textures after both conventional and asymmetric warm rolling.

ACKNOWLEDGEMENTS

CONFLICT OF INTEREST

On behalf of all authors, the corresponding author states that there is no conflict of interest.

REFERENCES

1. L. Kestens and S. Jacobs, *Text. Stress Microstruct.* 2008, 1 https://doi.org/10.1155/2008/173083 (2008).
2. H. Pirgazi, R.H. Petrov, and L.A.I. Kestens, *Steel Res. Int.* https://doi.org/10.1002/srin.201400608 (2016).
3. M.E. McHenry, *Encyclopedia of Materials: Science and Technology (Second Edition)*, ed. K.H.J. Buschow, W.C. Robert, C.F. Merton, I. Bernard, J.K. Edward, M. Subhash, and V. Patrick (Elsevier, Oxford, 2001), p. 8584.
4. B.D. Cullity and C.D. Graham, *Introduction to Magnetic Materials* (Wiley, New Jersey, 2011), p. 197.
5. P. Beckley, *Electrical Steels for Rotating Machines* (Institution of Engineering and Technology, London, 2002).
6. T. Tomida, *Mater. Trans.* 44, 1096–1105 https://doi.org/10.2320/matertrans.44.1096 (2003).
7. R.D. Doherty, D. Stojakovic, F.J.G. Landgraf, and S.R. Kalidindi, *Mater. Sci. Forum* 550, 497 https://doi.org/10.4028/www.scientific.net/MSF.550.497 (2007).
8. L. Kestens, J.J. Jonas, P. Van Houtte, and E. Aernoudt, *Text. Stress Microstruct.* 26–27, 321 https://doi.org/10.1155/TSM.26-27.321 (1996).
9. Y. Zhang, Y. Xu, H. Liu, C. Li, G. Cao, Z. Liu, and G. Wang, *J. Magn. Magn. Mater.* 324, 3328 https://doi.org/10.1016/j.jmmm.2012.05.046 (2012).
10. H.J. Bunge, *Texture Analysis in Materials Science—Mathematical Methods* (Butterworth & Co, Berlin, 1982).
11. G.I. Taylor, *J. Inst. Met.* 62, 307 (1938).
12. P. Van Houtte, S. Li, M. Seefeldt, and L. Delannay, *Int. J. Plast.* 21, 589 https://doi.org/10.1016/j.ijplas.2004.04.011 (2005).
13. L.S. Tóth and P. Van Houtte, *Texture Microstruct* 19, 229 https://doi.org/10.1155/tsm.19.229 (1992).
14. P. Van Houtte, *MTM-FHM Software User Manual, Ver. 2* (1995).
15. G.E. Dieter and D. Bacon, *Mechanical Metallurgy* (McGraw-Hill, New York, 1988), pp593–596.
16. D.N. Lee, *Mater. Sci. Forum* 449–452, 1 https://doi.org/10.4028/www.scientific.net/MSF.449-452.1 (2004).
17. S.-B. Kang, B.-K. Min, H.-W. Kim, D. Wilkinson, and J. Kang, *Metall. Mater. Trans. A Phys. Metall. Mater. Sci.* 36, 3141 https://doi.org/10.1007/s11661-005-0085-4 (2005).
18. J. Sidor, A. Miroux, R. Petrov, and L. Kestens, *Acta Mater.* 56, 2495 https://doi.org/10.1016/j.actamat.2008.01.042 (2008).
19. J. Gil Sevillano, P. van Houtte, and E. Aernoudt, *Prog. Mater. Sci.* 25, 69 https://doi.org/10.1016/0079-6425(80)90001-8 (1980).
20. A. Rollett, G.S. Rohrer, and J. Humphreys, *Recrystallization and Related Annealing Phenomena*, (2017), p. 1.
21. R.D. Doherty, D.A. Hughes, F.J. Humphreys, J.J. Jonas, D.J. Jensen, M.E. Kassner, W.E. King, T.R. McNelley, H.J. McQueen, and A.D. Rollett, *Mater. Sci. Eng. A* 238, 219 https://doi.org/10.1016/S0921-5093(97)00424-3 (1997).
22. B. Hutchinson, *Mater. Sci. Forum* 558–559, 13 https://doi.org/10.4028/www.scientific.net/MSF.558-559.13 (2007).
23. B. Hutchinson, *Philos. Trans. R. Soc. A Math. Phys. Eng. Sci.* 357, 1471 https://doi.org/10.1098/rsta.1999.0385 (1999).
24. N. Rajmohan, Y. Hayakawa, J.A. Szpunar, and J.H. Root, *Acta Mater.* 45, 2485 https://doi.org/10.1016/S1359-6454(96)00371-0 (1997).

25. P. Van Houtte, A.K. Kanjarla, A. Van Bael, M. Seefeldt, and L. Delannay, *Eur. J. Mech. A. Solids* 25, 634 https://doi.org/10.1016/j.euromechsol.2006.05.003 (2006).
26. G. Gottstein and L.S. Shvindlerman, *Grain Boundary Migration in Metals: Thermodynamics, Kinetics, Applications, Second Edition*, (2009), p. 1.
27. L. Kestens and J.J. Jonas, *Metall. Mater. Trans. A Phys. Metall. Mater. Sci.* 27, 155 https://doi.org/10.1007/BF02647756 (1996).
28. J.J. Sidor, R.H. Petrov, and L.A.I. Kestens, *Acta Mater.* 59, 5735 https://doi.org/10.1016/j.actamat.2011.05.050 (2011).
29. L.A.I. Kestens and H. Pirgazi, *Mater. Sci. Tech. Ser.* 32, 1303 https://doi.org/10.1080/02670836.2016.1231746 (2016).
30. M. Atake, M. Barnett, B. Hutchinson, and K. Ushioda, *Acta Mater.* 96, 410 https://doi.org/10.1016/j.actamat.2015.05.018 (2015).